



## Geometrical Shape Effects of Surface Texture on the Elastic Deformation in Soft-EHL Contacts

Binbin Su, Wei Huang & Xiaolei Wang

To cite this article: Binbin Su, Wei Huang & Xiaolei Wang (2019) Geometrical Shape Effects of Surface Texture on the Elastic Deformation in Soft-EHL Contacts, Tribology Transactions, 62:4, 592-602, DOI: [10.1080/10402004.2019.1586023](https://doi.org/10.1080/10402004.2019.1586023)

To link to this article: <https://doi.org/10.1080/10402004.2019.1586023>



Accepted author version posted online: 21 Mar 2019.  
Published online: 30 Apr 2019.



Submit your article to this journal [↗](#)



Article views: 72



View related articles [↗](#)



View Crossmark data [↗](#)



# Geometrical Shape Effects of Surface Texture on the Elastic Deformation in Soft-EHL Contacts

Binbin Su, Wei Huang, and Xiaolei Wang

National Key Laboratory of Science and Technology on Helicopter Transmission, Nanjing University of Aeronautics and Astronautics, Nanjing, P. R. China

## ABSTRACT

In order to investigate the elastic deformation behavior of surface texture on sliding bearings with relatively soft material under lubricated condition, observation on the deformed surface around the dimple patterns, including circular, elliptical, triangular, quadrangular, and diamond, is performed by optical interferometry. Comparison of elastic deformation around different geometrical shaped dimples is conducted. The results indicate that the geometrical shape of the dimple has obvious influence on the elastic deformation of the textured surface; both the maximum and scope of deformation are closely related to the geometrical shape of the dimple. The geometrical shape effect becomes increasingly remarkable with growth of applied load. Finally, the optimum geometrical shape of surface texture for soft-EHL contacts with respect to the minimum elastic deformation is obtained.

## ARTICLE HISTORY

Received 20 April 2018  
Accepted 19 February 2019

## KEYWORDS

Surface texture; geometrical shape; elastic deformation; soft-EHL contacts

## Introduction


Reliable and stable surface texture is essential to obtain the optimum tribological properties of tribo-contacts (1–5). Currently, most of the important texturing parameters, including depth-to-diameter ratio, area ratio, and texture size, have been extensively investigated through both theoretical and experimental methods (6–10).

In addition, the geometrical shape is another critical issue for the design of surface texture. The effect of the geometrical shape of surface texture on tribological behaviors has also been studied (11–14). Elliptical dimples with the major axis placed perpendicular to the sliding direction was theoretically found to perform better in regard to load-carrying capacity (15, 16) and was experimentally verified to show lower friction coefficient between conformal contacting surface (17). Similar results were obtained in the gas-lubricated parallel slider bearings textured by ellipsoidal shape concave (18, 19). With the development of computer technology and numerical simulation, various approaches for textural shape optimization have emerged and outputted several novel geometrical shapes for surface texture, such as the chevron-like dimple shape (20) obtained by the Successive Quadratic Programming (SQP) algorithm and the fish-shaped textures (21) based on the Genetic Algorithm (GA) algorithm.

However, the optimized geometrical shape of the surface texture revealed in the aforementioned research studies may not be suitable for tribo-contacts made of relatively soft materials, in which the elastic deformation of the contacting

surface cannot be ignored. Numerous studies (22–27) have indicated that surface elastic deformation is playing an increasingly important role in the performance of tribo-contacts, especially for those made of relatively soft materials, such as plastics and rubber. During a more generalized optimization of texturing parameters, the optimal dimple area density in regard to low friction on the surface of ultra-high-molecular-weight polyethylene (UHMWPE) obviously differs from that on the relatively rigid surface of steel (28, 29). Hence, more attention should be paid to elastic deformation when studying the geometrical shape effects of surface texture on tribological performance in soft contacts.

It interesting to question whether the deformation is always bad for lubricated contacts. First, the maximum hydrodynamic pressure is the most important design criterion of surface texture for tribo-contacts under liquid lubrication. From this perspective, deformation may result in the deviation from initial design intention, deteriorating the hydrodynamic effect of surface texture (22, 30–34) by changing the optimized geometry of the textured surface. Second, deformation always emerges at a high pressure zone, making the high-pressure fluid prone to leakage, so that it seems difficult to have the surface texture achieve the best geometry after deformation. On the other hand, deformation may cause the rise of a partial area, which decreases the flatness of the surface and decrease the film thickness of hydrodynamic lubrication. Therefore, there seem to be more reasons to minimize the deformation of soft contacts in order to maximize the hydrodynamic effect of surface texture.

CONTACT Xiaolei Wang  [wxl@nuaa.edu.cn](mailto:wxl@nuaa.edu.cn)

Color versions of one or more of the figures in the article can be found online at [www.tandfonline.com/utrb](http://www.tandfonline.com/utrb).

Review led by Yeau-Ren Jeng.

Different geometry of the surface texture may have different deformation behavior. In order to experimentally investigate the effect of geometrical shape of dimple on the elastic deformation of textured surface, this article presents observations on the deformed surface textured by dimple with various geometrical shapes through using optical interferometry. The soft tribo-contacts consist of a flat glass and dimpled polydimethylsiloxane (PDMS) sliders. Commonly used geometrical shape of surface texture, including circular, elliptical, triangular, quadrangular and diamond-shaped dimples, are fabricated on the soft surface of PDMS sliders. Interferometric images and their corresponding elastic deformation across the contacting areas under various applied loads are reported. The optimum geometrical shape of surface texture for soft-EHL contacts is suggested in regard to the minimum elastic deformation.

## Experimental Details

A customized optical slider-on-disc test instrument (35) based on the principle of interferometry is used in this study to observe the deformed surface across soft-EHL contacts. As schematically illustrated in Fig. 1, the soft-EHL contact, which is submerged in simethicone with viscosity of 485 mPa·s (26 °C), consists of a fixed-incline elastic slider made of PDMS and a rotating transparent BK7 glass disk. The PDMS slider comes into contacting with an initial inclination angle  $\alpha$  of 0.08 rad in order to ensure the entrainment of the lubricant into the soft contacts. A conventional monochromatic red light with wavelength of 650 nm is adopted as incident illumination. More detailed information about the test procedure is available in our previous study (36).

The soft slider is made of polydimethylsiloxane prepolymer (including the PDMS monomer and curing agent), a kind of commercially available elastomer. The properties of the final PDMS sliders samples used in the observation are listed in Table 1. As shown in Table 1, the longer side of the observing surface is oriented perpendicularly to the flow direction of lubricant.

A micro-dimple with certain geometrical shape is fabricated at the observing surface center of the PDMS slider by lithography and replica technique during the mould procedure, as described in detail earlier (37). In order to distinguish the effect of dimple shape, all designed textures with various geometrical shapes have the same depth and equivalent area, as shown in Table 2. Dimples are all situated inside the converging gap with their centroids overlapped on that of the observing surfaces. Dimple morphology measured with a white-light interfering three-dimensional (3D) profilometer is also presented in Table 2.

In order for high-quality interference fringes, a chemical deposit approach (38) is employed to coat a silver layer with thickness of about 20 nm on the PDMS surface. The final chemically deposited PDMS slider sample (displayed in brown), as well as the sectional profile of dimple, is presented in Fig. 2. The sectional profile of dimple obviously indicates that the designed morphology of the surface

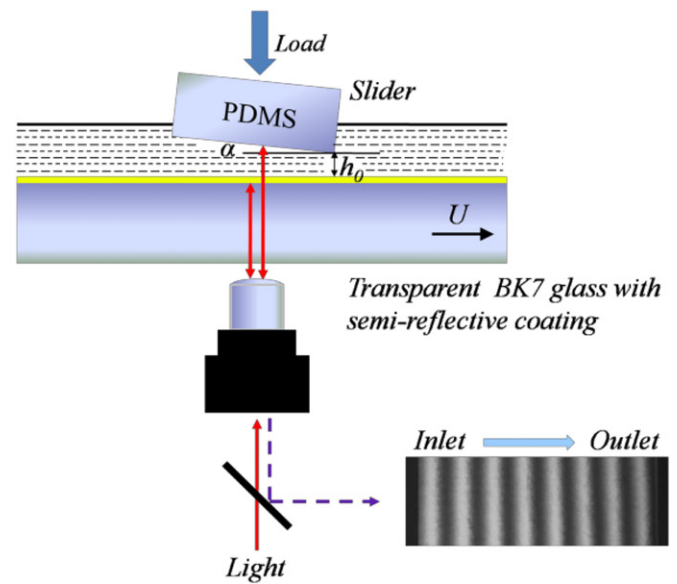
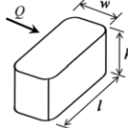


Figure 1. Schematic of the slider-on-disc setup using optical interferometry.

Table 1. Properties of the PDMS slider samples.

Material	Orientation	Dimension $l \times w \times h$	Surface roughness	Young modulus	Poisson's ratio
PDMS		$12 \times 5 \times 10 \text{ mm}^3$	$R_a < 10 \text{ nm}$	1.036 MPa	0.49

texture is not affected by the deposited Ag coating, which is experimentally found to markedly improve the light reflection performance of the PDMS slider sample.

All the observations on contacting surface are carried out under the controlled environmental conditions with constant room temperature of 26 °C. All interferograms are collected when the oil lubrication is stabilized. Major testing parameters are summarized in Table 3.

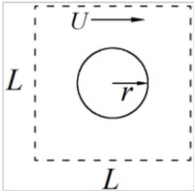
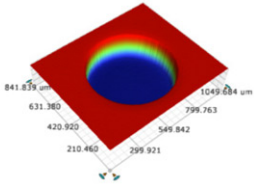
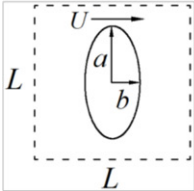
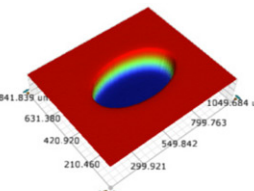
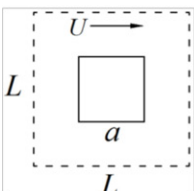
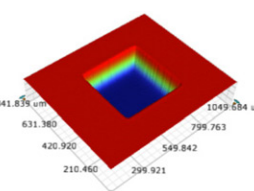
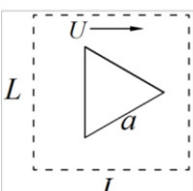
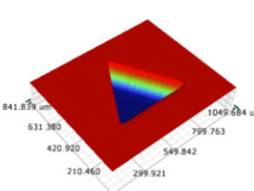
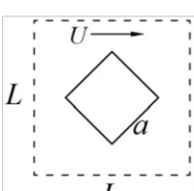
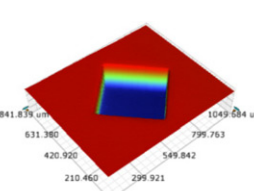
## Results and discussions

The interferograms around the dimple in soft-EHL contacts and its variation along with applied load are summarized; in addition, corresponding sketches of deformed surface to typical interferograms are also presented, as described in the following.

### Light load

The typical interferograms around the dimple with different geometrical shapes under the condition of light load  $F = 3.92 \text{ N}$  and  $U = 7.854 \text{ mm/s}$  are presented in Fig. 3. In these and the following interferograms, the inlets of the lubricant locate at the left of figures, with the direction of main entrainment labeled by a yellow arrow. Under the light load condition, owing to the initial inclination angle of the soft slider, the slider surface at the trailing edge of the

**Table 2.** Geometry parameters of the patterns of dimples.

Geometrical shape	Dimple Morphology	Description	Depth	Parameter
		Circle	5 $\mu\text{m}$	$r = 300 \mu\text{m}$
		Ellipse ( $a = 2b$ )	5 $\mu\text{m}$	$b = 212.132 \mu\text{m}$ $a = 424.264 \mu\text{m}$
		Quadrat	5 $\mu\text{m}$	$a = 531.601 \mu\text{m}$
		Triangle	5 $\mu\text{m}$	$a = 807.859 \mu\text{m}$
		Diamond	5 $\mu\text{m}$	$a = 531.601 \mu\text{m}$

dimple (right part of the interferograms) comes into contacting status preferentially, while a small gap is reserved at the leading edge of the dimple (left part of the interferograms), which makes the interference fringes dim, undistinguishable, and unable to be detected by the charge-coupled device (CCD) camera because of the thick lubricant film, as labeled by the red dotted line in Fig. 3 a.

As shown clearly by the pictures, all the fringes at the trailing edge of the dimples roughly keep the same pattern and bend upstream regardless of the dimple shape. In order to visualize the deformed surface around the dimples approximately, the sketch based on the interferograms is drawn as shown in Fig. 3b, in which the yellow arrow represents the direction of main entrainment. The typical interferograms around the dimple with different geometrical shapes are so similar that just the corresponding sketch of the circular dimpled surface is given.

By common sense, around the convergent part of dimple, the surface nearby would be concave owing to the effect of hydrodynamic pressure, according to usual cognition. However, as reflected by the sketch in Fig. 3b, the fringes at the trailing edge of the dimple indicate the surface nearby becomes convex. Under light load, the PDMS slider and glass disc generate a convergent wedge, as shown in Fig. 4, and interference fringes bend toward the inlet of the contact; according to the principle of equal thickness interference, it can be easy to judge the convex deformation at the trailing edge of the dimple.

In the current case, on one hand, the thickness of lubricant film is much larger than the depth of the dimple with the light load on the slider, so the hydrodynamic effect on the surface texture is extremely small. On the other hand, the dimple is not completely inside the contacting area, and the divergent part of the dimple has a good exposure to the inlet ambient owing to the existence of initial slider

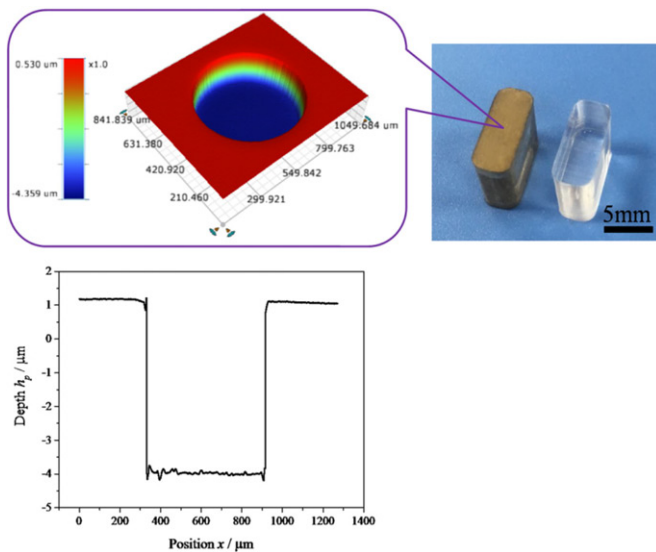


**Figure 2.** Photographic image and 3D profile of the textured PDMS slider sample with chemically deposited Ag coating.

**Table 3.** Testing parameters.

Item	Value
Load $F$	1.96–19.6 N
Mean pressure $P$	0.032–0.32 MPa
Sliding velocity $U$	7.854 mm/s
Initial inclination angle $\alpha$	0.08 rad
Viscosity of lubricant $\eta_0$	485 mPa·s (26 °C)
Atmosphere pressure $P_a$	$1 \times 10^5$ Pa
Cavitation pressure $P_{cav}$	$1 \times 10^5$ Pa
Initial film thickness in simulation $h_0$	$5 \mu\text{m}$

inclination and elastic deformation, which implies the low pressure zone in the divergent part of the dimple would be limited. Consequently, Poiseuille flow, which sucks lubricant into the contacting area, presents to be slight; then, the hydrodynamic pressure around the convergent part of the dimple would be tiny and would have a weak effect on total deformation. The effect of viscous shear stress caused by Couette flow will play the main role in the total deformation and finally lead to a convex surface.

Although the deformation at the trailing edge of various shaped dimples presents the same pattern of “convex” as shown in Fig. 3a, the degrees of deformation are different and can be reflected by the density and bending intensity of the interference fringes. It is noticeable that the fringes at the trailing edge of triangular dimple distribute rather closely and bend more severely, meaning a larger elastic deformation. Owing to the rapidly converging sharp angle of the triangle along the sliding direction on a two-dimensional plane, the Couette flow across the dimple driven by the sliding surface will gather at the sharp-angled convergent edge and lead to a more serious viscous shear stress, which finally induces a larger elastic deformation. On the contrary, much more gently does the Couette flow pass the elliptical dimple as the longest transverse and slowly converging edge, resulting in relatively alleviated deformation.

Figure 5 shows a sequence of interferograms around the dimple with different geometrical shapes at the constant sliding velocity of 7.854 mm/s and various light load of 1.96–5.88 N. The figures clearly show that all the fringes near the trailing

edge of the dimple, regardless of the geometrical shape, roughly keep the same trend of bending upstream. In the meantime, the fringes near the leading edge of dimple become increasingly detectable by the CCD camera as the lubricant film thickness decreases gradually with the growth of applied load  $F$ .

Furthermore, the bending of the fringes at the trailing edge of the dimple is readily found to become increasingly severe first and then alleviated, as shown in Fig. 5. With the growth of applied load, the increasing bending and density of fringes can be attributed to the increasingly aggravated effect of shear strain caused by Couette flow with the decrease of lubricant film thickness; meanwhile, the compressive strain caused by hydrodynamic pressure becomes gradually obvious and serves to alleviate the bending of the fringes.

### Medium load

The typical interferograms around the dimple with different geometrical shapes under the condition of medium load  $F = 13.72$  N and  $U = 7.854$  mm/s are presented in Fig. 6. In this case, the dimple completely steps into the contacting area, and the film thickness across the soft contacts decreases as a larger load on the slider, so the interference fringes across the dimpled surface can be clearly detected by the CCD camera. One of the most prominent characteristics of the interferograms is the emergence of the mushroom-shaped fringes around the dimple.

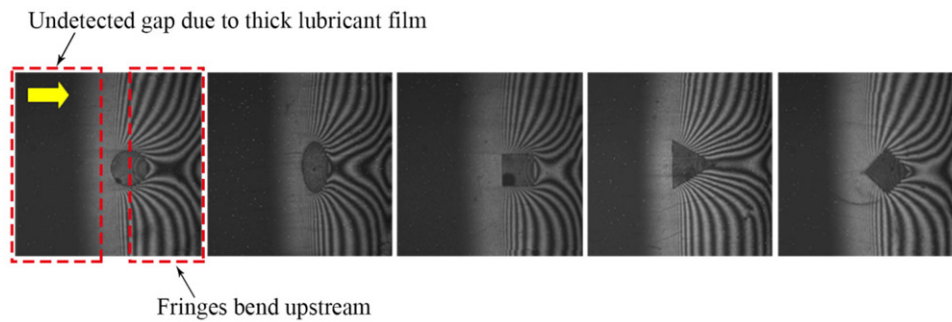
As depicted by the sketch in Fig. 6b, the mushroom-shaped fringes imply concave deformation around the dimple. The interference intensity  $I$  for bright fringes versus the film thickness  $h$  follows a negative correlation (35),

$$I \propto I_0 e^{-\alpha h} \quad [1]$$

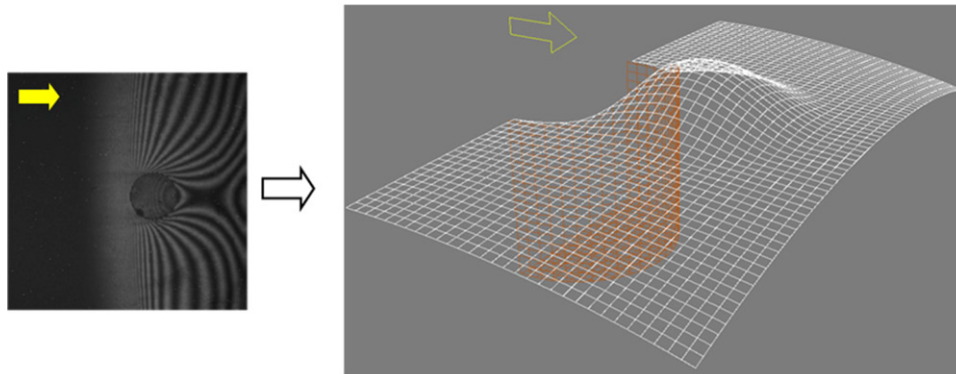
where  $I_0$  is the intensity of incident light and  $\alpha$  is the light absorption coefficient for lubricant oil; the detailed derivation for Eq. [1] is presented in the appendix. Resorting to the relationship in Eq. [1], the deformation pattern around the dimple can be judged through the comparison of the interference intensity  $I$  for bright fringes. Under medium load, interference intensity distribution across the dimple is shown in Fig. 7. The interference intensity for bright fringes at regions A, B, and C are labeled, and this clearly shows that the interference intensity for bright fringes at region A is higher than those at regions B and C. Thus, the films at regions B and C are thicker, which implies a concave surface nearby based on the flat surface of region A, as depicted by the sketch in Fig. 6b.

The mechanism of the concave surface can be explained as follows: The soft surface around the convergent part of the dimple is positively depressed owing to the generated hydrodynamic pressure, while the divergent step wedge is tangentially stretched and collapsed owing to the effect of viscous shear strain. In this case, a low pressure zone emerges at the divergent part of dimple; the pressure difference between the inlet ambient and low pressure zone induces obvious Poiseuille flow owing to the effect of “inlet suction” proposed by Olver et al. (39, 40), which is the main generation mechanism for the additional hydrodynamic pressure around the convergent part of dimples. Owing to





(a) Typical interferograms of deformed surface around the various shaped dimples.



(b) Corresponding sketch of deformed surface around the circular dimple.

**Figure 3.** Typical interferograms and corresponding sketch of deformed surface around the dimple with different geometrical shapes under light load  $F = 3.92$  N and  $U = 7.854$  mm/s.

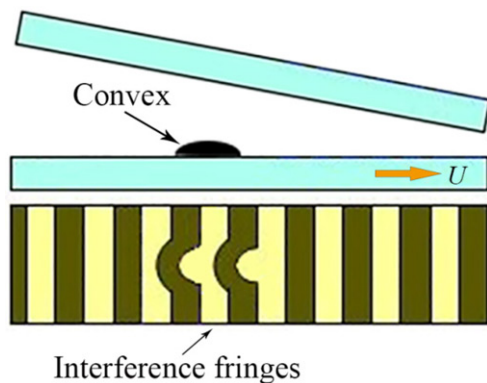


**Figure 4.** Equal thickness interference formed by the convergent wedge.

the thinner lubricant film, the effect of viscous shear strain caused by Couette flow plays a main role in the total deformation around the divergent part of the dimples.

It is clearly displayed in Fig. 6a that the sparsest fringes, as well as the minimum occupied region, appear at the trailing edge of elliptical dimple, which indicates the most alleviative deformation nearby. Instead, the reverse happens on the triangular dimpled surface, along with the severest deformation at the trailing edge. As the positive deformation closely depends on the hydrodynamic pressure generated around the convergent parts of dimple, it is necessary to analyze the pressure distribution across the textured contacts in order to explain the geometrical shape effect of dimple on the elastic deformation. Figure 8 presents the pressure

distribution of the elliptical and triangular dimples obtained by numerical simulation with identical operating conditions (initial film thickness  $h_0 = 5 \mu\text{m}$ ); the direction of main entrainment speed is from left to right in the figure, and it is easy to recognize that when the pressure builds up along the converging edge of the dimple, high pressure at the trailing edge of triangular dimple becomes much more concentrated around the sharp corner owing to a confluent Poiseuille flow and results in a larger deformation nearby. Decentralized high pressure arises in an elliptical dimpled surface and lead to a smaller deformation finally.

Figure 9 shows a sequence of interferograms around the dimple with different geometrical shapes at the constant sliding velocity of 7.854 mm/s and various medium loads of 10.78–14.7 N. With the growth of applied load  $F$ , the interferograms around a certain shape of dimple keep basically similar, but an increasing number of closed fringes emerge at the leading edge of the dimples owing to the increasing Couette shear stress caused by decreasing film thickness; in the meantime, the interference fringes at the trailing edge of the dimples keeps increasing and expanding outward, which is induced by an increasing Poiseuille flow across the convergent part of dimple because of the lowering pressure at the divergent zone of the dimple.

### Heavy load

The typical interferograms around the dimple with different geometrical shapes under the condition of heavy load

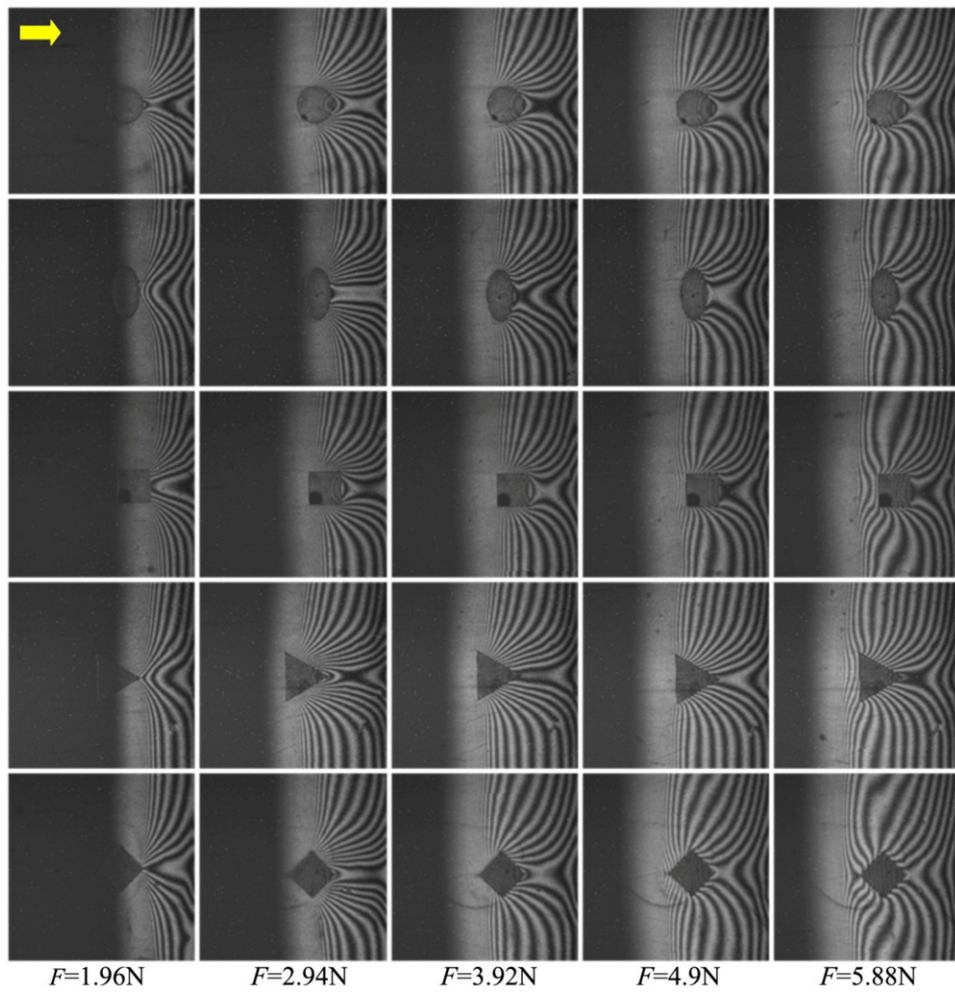
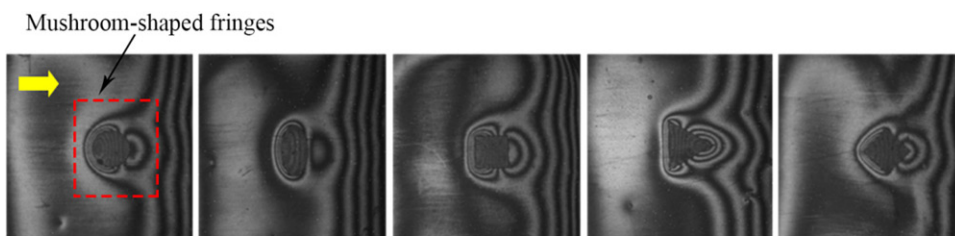
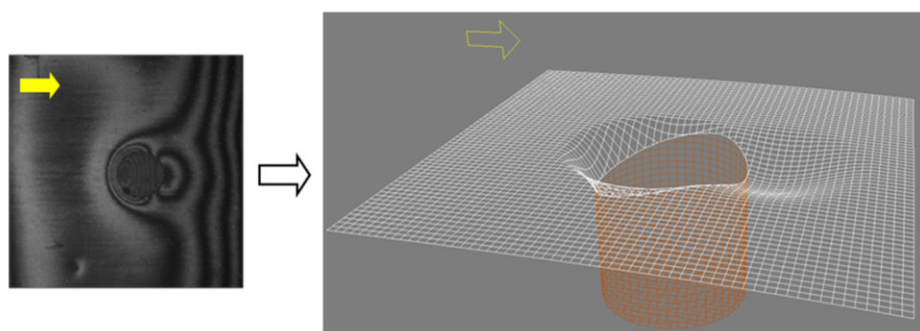


Figure 5. Optical interferograms around the dimple with different geometrical shapes for various light load  $F$  at a constant sliding velocity of 7.854 mm/s.



(a) Typical interferograms of deformed surface around the various shaped dimples.



(b) Corresponding sketch of deformed surface around the circular dimple.

Figure 6. Typical interferograms and corresponding sketch of deformed surface around the dimple with different geometrical shapes under medium load  $F = 13.72$  N and  $U = 7.854$  mm/s.

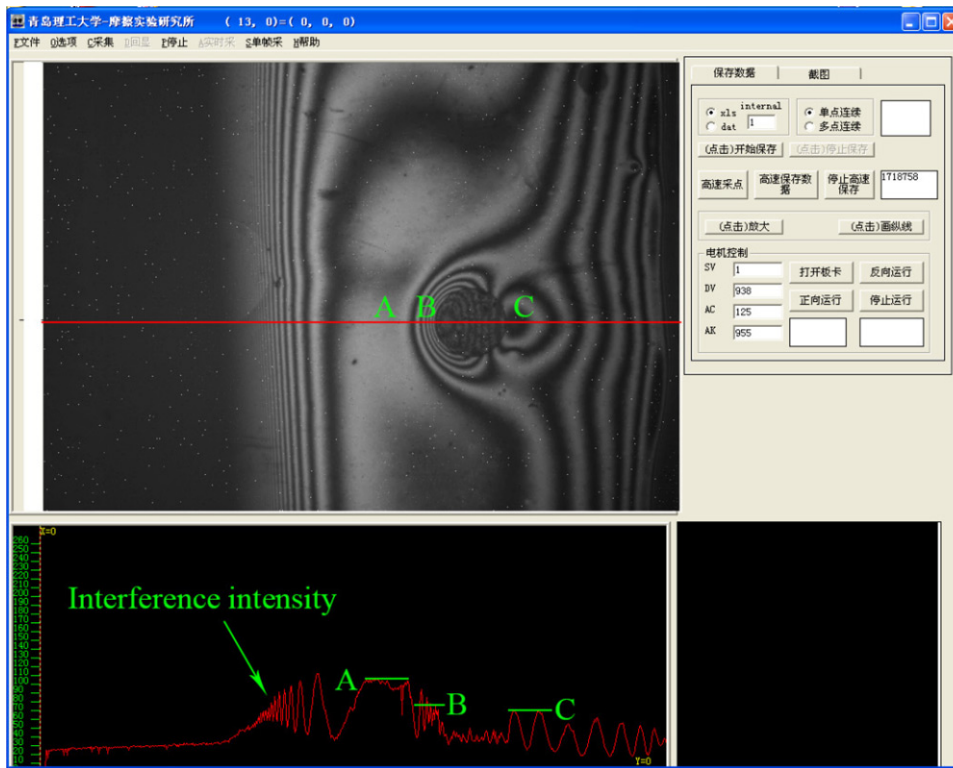


Figure 7. Interference intensity distribution across the dimple under medium load.

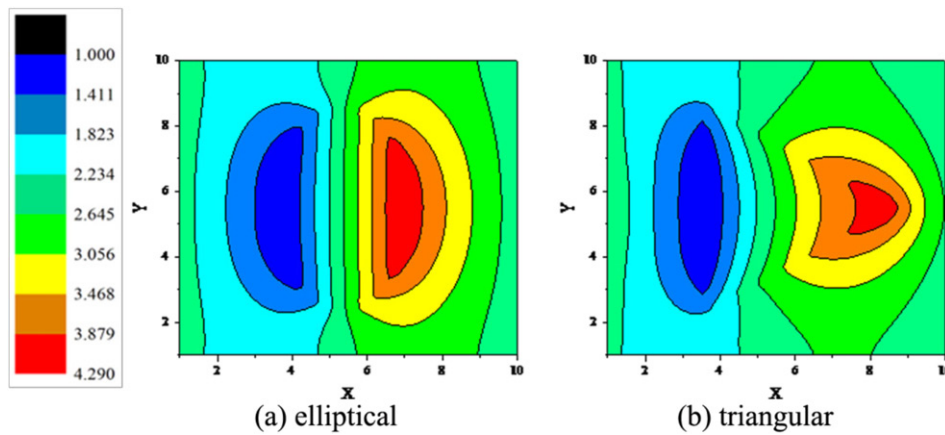


Figure 8. Pressure distribution of different shaped dimples obtained by numerical simulation.

$F = 18.62$  N and  $U = 7.854$  mm/s, as well as the corresponding sketch of the deformed surface, are presented in Fig. 10. In addition to the mushroom-shaped fringes appearing around the dimple, another interesting finding is the emergence of the new crescent-shaped fringes at the upstream of the dimple.

Compared with those under medium applied load, the fringes at the trailing edge of the dimples become much denser owing to the increasing effect of hydrodynamic pressure and their corresponding scopes expand outward consistently, while the fringes at the leading edge of the dimples are compressed into a limited scope. In addition to the depressed deformation occupied by the mushroom-shaped fringes around the dimples, special attention deserves to be given to the protuberances, which correspond to the crescent-shaped fringes at the upstream of the dimples, caused by

the stacking of materials as a result of the much more serious Couette shear stress, as shown in the sketch in Fig. 10b.

Similarly, the already-mentioned deformation also can be judged through the comparison of the interference intensity for bright fringes. Figure 11 presents the interference intensity distribution across the dimple under heavy load. The interference intensity for bright fringes at regions A, B, C, and D can easily reflect the deformation pattern around the dimple, based on the flat surface of region A, the “crescent-shape” protuberance that emerges at region B, and the distorted “mushroom-shape” concave effect at regions C and D, as depicted by the sketch in Fig. 10b.

As shown clearly in Fig. 10a, the sparsest fringes still appear at the trailing edge of the elliptical dimple, which indicates the most alleviative deformation nearby. In addition to the sparse fringes, the location offset of the



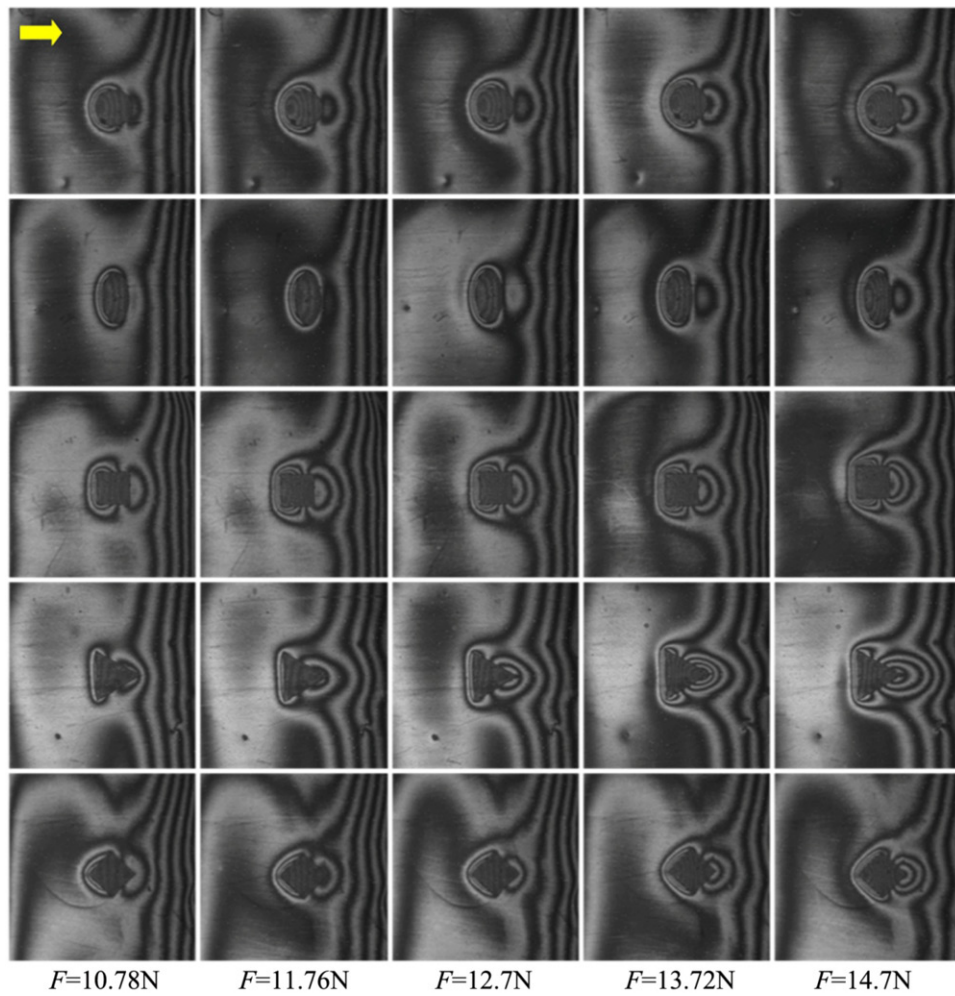
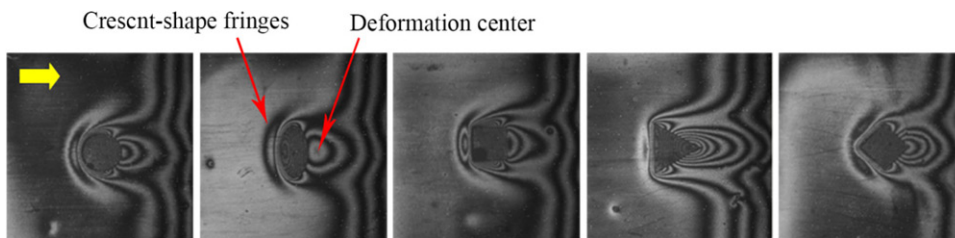
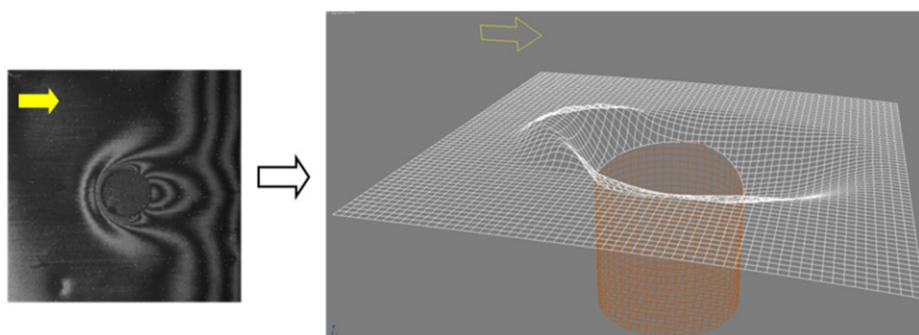


**Figure 9.** Optical interferograms around the dimple with different geometrical shapes for various applied medium loads  $F$  at a constant sliding velocity of 7.854 mm/s.



(a) Typical interferograms of deformed surface around the various shaped dimples.



(b) Corresponding sketch of deformed surface around the circular dimple.

**Figure 10.** Typical interferograms and corresponding sketch of deformed surface around the dimple with different geometrical shapes under heavy load,  $F = 18.62$  N and  $U = 7.854$  mm/s.

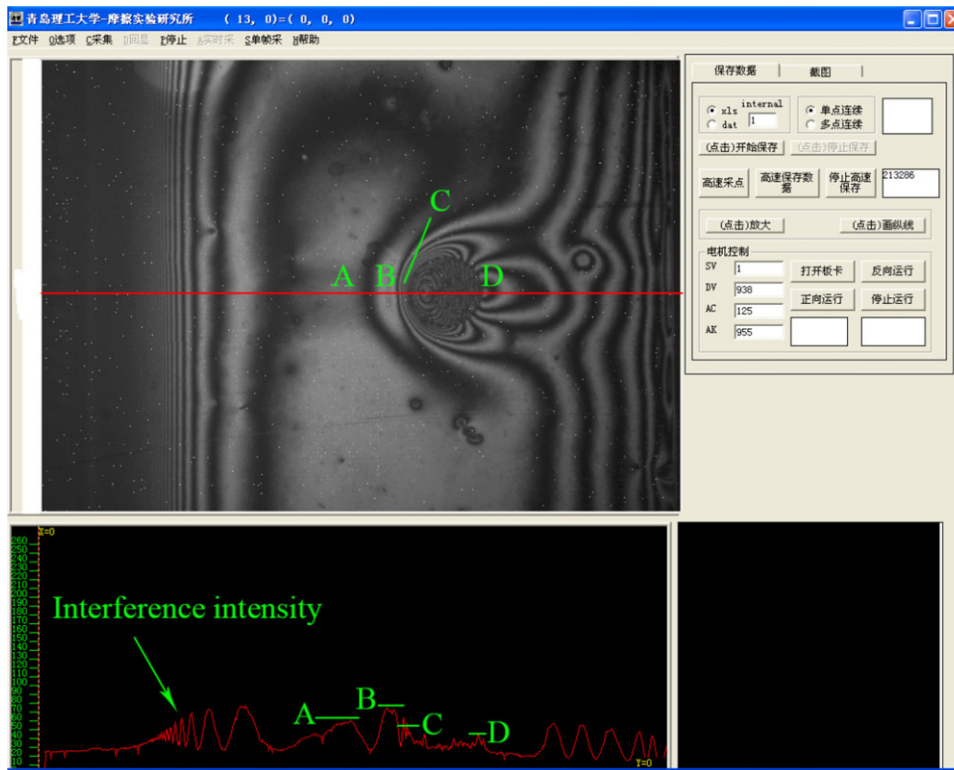


Figure 11. Interference intensity distribution across the dimple under heavy load.

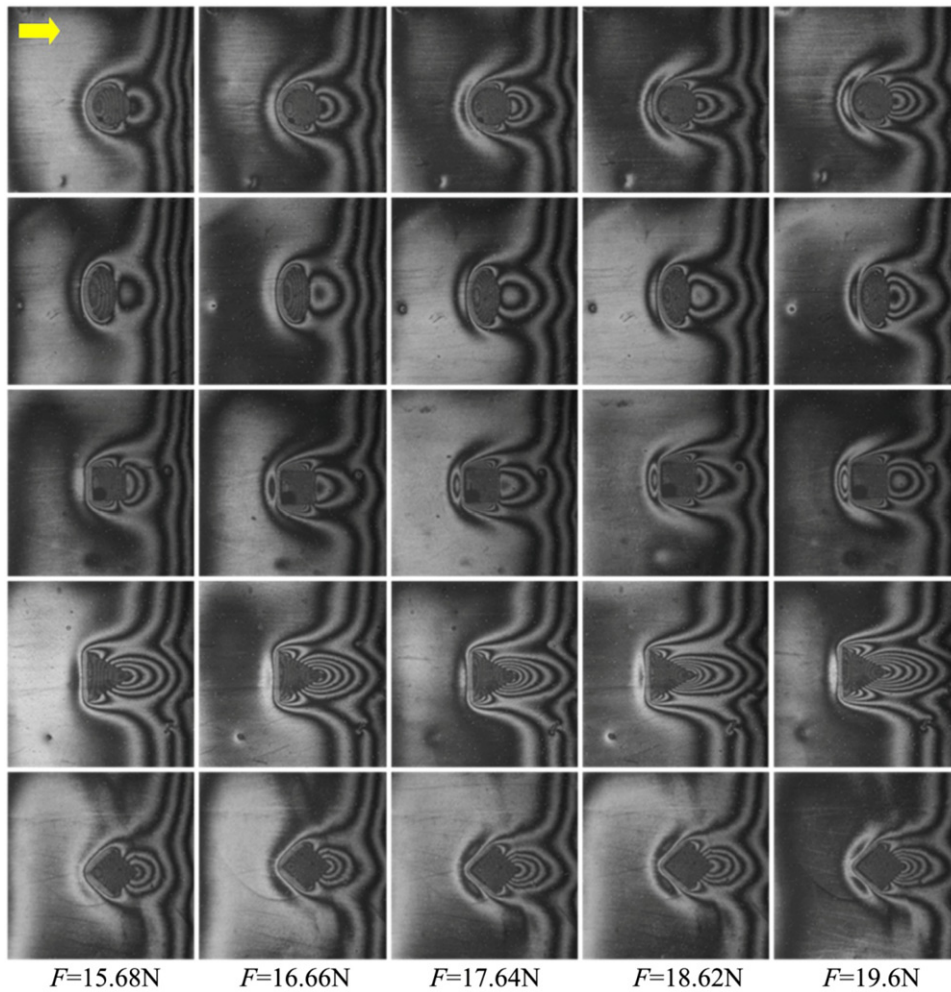


Figure 12. Optical interferograms around the dimple with different geometrical shapes for various applied heavy loads  $F$  at a constant sliding velocity of 7.854 mm/s.

maximum deformation at the trailing edge of the elliptical dimple caused by a more severe Couette shear stress presents much more distinctly than that under the condition of medium applied load, as pointed out in Fig. 10a. Instead, the severest deformation revealed by the densest and expanding fringes emerges at the trailing edge of the triangular dimple due to the confluent Poiseuille flow.

Figure 12 shows a sequence of interferograms around the dimple with different geometrical shapes at a constant sliding velocity of 7.854 mm/s and various heavy loads of 15.68–19.6 N. Except for the increasing closed fringes at the leading and trailing edges of the dimples, protuberances caused by the shear strain at the upstream of the dimples become increasingly obvious along with the growth of applied load. Furthermore, the scope of fringes constantly expands at the trailing edge of dimples while condensing at the leading edge.

## Conclusion

The experimental observation on the deformed surface around various shaped dimples, including circular, elliptical, triangular, quadrangular, and diamond, was carried out in soft-EHL contacts by using optical interferometry. The following are the key conclusions drawn from the present study:

1. The pattern of elastic deformation around dimple in soft-EHL contacts changes along with the applied load. Under a certain type of applied load, the patterns of elastic deformation around the dimple are basically similar regardless of the geometrical shape of dimple. However, owing to the different hydrodynamic pressure distribution and local structural rigidity induced by various dimple shapes, the degree of deformation, including the maximum and deformed scope, closely depends on the geometrical shape of dimple. Furthermore, the geometrical shape effect of surface texture on deformation degree becomes increasingly remarkable as the growth of applied load.
2. For maximum hydrodynamic effect of the surface texture, the elliptical dimple with major axis perpendicular to the sliding direction is recommended to be the optimum geometrical shape of surface texture in soft-EHL contacts. A textural shape with sharp-angled converging edge, such as a triangular and a diamond dimple, induces more severe deformation and should be avoided in surface texture design.

## Acknowledgements

This article is based on research work supported by the National Nature Science Foundation of China (NSFC) (51675268).

## References

- (1) Ma, C., and Zhu, H. (2011), "An Optimum Design Model for Textured Surface With Elliptical-Shape Dimples Under Hydrodynamic Lubrication," *Tribology International*, **44**(9), 987–995.
- (2) Bounif, A., Fillon, M., Maspeyrot, P., and Tala-Ighil, N. (2007), "Effects of Surface Texture on Journal-Bearing Characteristics Under Steady-State Operating Conditions," *Proceedings of the Institution of Mechanical Engineers, Part J: Journal of Engineering Tribology*, **221**(6), 623–633.
- (3) Wang, X. L., Kate, K., and Adachi, K. (2001), "The Effect of Laser Texturing of SiC Surface on the Critical Load for Transition of Water Lubrication Mode From Hydrodynamic to Mixed," *Tribology International*, **34**(10), 703–711.
- (4) Yan, D., Qu, N., Li, H., and Wang, X. (2010), "Significance of Dimple Parameters on the Friction of Sliding Surfaces Investigated by Orthogonal Experiments," *Tribology Transactions*, **53**(5), 703–712.
- (5) Etsion, I. (2004), "Improving Tribological Performance of Mechanical Components by Laser Surface Texturing," *Tribology Letters*, **17**(4), 733–737.
- (6) Etsion, I., and Burstein, L. (1996), "A Model for Mechanical Seals with Regular Microsurface Structure," *Tribology Transactions*, **39**(3), 677–683.
- (7) Brizmer, V., Kligerman, Y., and Etsion, I. (2003), "A Laser Surface Textured Parallel Thrust Bearing," *Tribology Transactions*, **46**(3), 397–403.
- (8) Wang, X. L., Kate, K., Adachi, K., and Aizawa, K. (2003), "Loads Carrying Capacity Map for the surface Texture Design of SiC Thrust Bearing Sliding in Water," *Tribology International*, **36**(3), 189–197.
- (9) Wang, X., Adachi, K., Otsuka, K., and Kato, K. (2006), "Optimization of the Surface Texture for Silicon Carbide Sliding in Water," *Applied Surface Science*, **253**(3), 1282–1286.
- (10) Sperka, P., Krupka, I., and Hartl, M. (2016), "The Effect of Surface Grooves on Film Breakdowns in Point Contacts," *Tribology International*, **102**, 249–256.
- (11) Imai, N., and Kato, T. (2013), "Effects of texture patterns on hydrodynamic and mixed lubrication characteristics," *Proceedings of the Institution of Mechanical Engineers, Part J: Journal of Engineering Tribology*, **227**(8), 898–904.
- (12) Wang, X., Giovannini, M., Xing, Y., Kang, M., and Ehmann, K. (2015), "Fabrication and Tribological Behaviors of Corner-Cube-Like Dimple Arrays Produced by Laser Surface Texturing on Medical Needles," *Tribology International*, **92**, 553–558.
- (13) Uddin, M. S., Ibatan, T., and Shankar, S. (2017), "Influence of Surface Texture Shape, Geometry and Orientation on Hydrodynamic Lubrication Performance of Plane-to-Plane Slider Surfaces," *Lubrication Science*, **29**(3), 153–181.
- (14) Lu, P., Wood, R. J. K., Gee, M. G., Wang, L., and Pflöging, W. (2018), "A Novel Surface Texture Shape for Directional Friction Control," *Tribology Letters*, **66**(1).
- (15) Yu, H., Wang, X., and Zhou, F. (2010), "Geometric Shape Effects of Surface Texture on the Generation of Hydrodynamic Pressure Between Conformal Contacting Surfaces," *Tribology Letters*, **37**(2), 123–130.
- (16) Yu, H., Huang, W., and Wang, X. (2013), "Dimple Patterns Design for Different Circumstances," *Lubrication Science*, **25**(2), 67–78.
- (17) Yu, H., Deng, H., Huang, W., and Wang, X. (2011), "The Effect of Dimple Shapes on Friction of Parallel Surfaces," *Proceedings of the Institution of Mechanical Engineers, Part J: Journal of Engineering Tribology*, **225**(8), 693–703.
- (18) Qiu, M., Delic, A., and Raeymaekers, B. (2012), "The Effect of Texture Shape on the Load-Carrying Capacity of Gas-Lubricated Parallel Slider Bearings," *Tribology Letters*, **48**(3), 315–327.
- (19) Qiu, M., Minson, B. R., and Raeymaekers, B. (2013), "The Effect of Texture Shape on the Friction Coefficient and Stiffness of Gas-Lubricated Parallel Slider Bearings," *Tribology International*, **67**, 278–288.
- (20) Shen, C., and Khonsari, M. M. (2016), "Texture Shape Optimization for Seal-Like Parallel Surfaces: Theory and Experiment," *Tribology Transactions*, **59**(4), 698–706.



- (21) Zhang, H., Hua, M., Dong, G.-Z., Zhang, D.-Y., Chen, W.-J., and Dong, G.-N. (2017), "Optimization of Texture Shape Based on Genetic Algorithm Under Unidirectional Sliding," *Tribology International*, **115**, 222–232.
- (22) Choudhury, D., Roy, T., Krupka, I., Hartl, M., and Mootanah, R. (2014), "Tribological Investigation of Ultra-High Molecular Weight Polyethylene Against Advanced Ceramic Surfaces in Total Hip Joint Replacement," *Proceedings of the Institution of Mechanical Engineers, Part J: Journal of Engineering Tribology*, **229**(4), 410–419.
- (23) Maeda, N., Chen, N., Tirrell, M., and Israelachvili, J. N. (2002), "Adhesion and Friction Mechanisms of Polymer-on-Polymer Surfaces," *Science*, **297**, 379–382.
- (24) Thatte, A., and Salant, R. F. (2012), "Effects of Multi-Scale Viscoelasticity of Polymers on High-Pressure, High-Frequency Sealing Dynamics," *Tribology International*, **52**, 75–86.
- (25) Li, F., Zhang, G., Wang, A., and Guo, F. (2017), "The Effects of Surface Mechanical Deformation and Bovine Serum Albumin on the Tribological Properties of Polyvinyl Alcohol Hydrogel as an Artificial Cartilage," *Advances in Materials Science and Engineering*, **2017**, 1–9.
- (26) Yagi, K., and Sugimura, J. (2013), "Elastohydrodynamic Simulation of Rayleigh Step Bearings in Thin Film Hydrodynamic Lubrication," *Tribology International*, **64**, 204–214.
- (27) Yagi, K., and Sugimura, J. (2013), "Elastic Deformation in Thin Film Hydrodynamic Lubrication," *Tribology International*, **59**, 170–180.
- (28) Zhang, B., Huang, W., Wang, J., and Wang, X. (2013), "Comparison of the Effects of Surface Texture on the Surfaces of Steel and UHMWPE," *Tribology International*, **65**, 138–145.
- (29) Wang, X., Wang, J., Zhang, B., and Huang, W. (2015), "Design Principles for the Area Density of Dimple Patterns," *Proceedings of the Institution of Mechanical Engineers, Part J: Journal of Engineering Tribology*, **229**(4), 538–546.
- (30) Shinkarenko, A., Kligerman, Y., and Etsion, I. (2009), "The Effect of Elastomer Surface Texturing in Soft Elasto-Hydrodynamic Lubrication," *Tribology Letters*, **36**(2), 95–103.
- (31) Shinkarenko, A., Kligerman, Y., and Etsion, I. (2010), "The Effect of Surface Texturing in Soft Elasto-Hydrodynamic Lubrication," *Tribology International*, **42**(2), 284–292.
- (32) Shinkarenko, A., Kligerman, Y., and Etsion, I. (2010), "Theoretical Analysis of Surface-Textured Elastomer Sleeve in Lubricated Rotary Sliding," *Tribology Transactions*, **53**(3), 376–385.
- (33) Su, B., Huang, L., Huang, W., and Wang, X. (2017), "The Load Carrying Capacity of Textured Sliding Bearings With Elastic Deformation," *Tribology International*, **109**, 86–96.
- (34) Young, S. K., Lotito, M. A., and Keller, T. S. (1998), "Friction Reduction in Total Joint Arthroplasty," *Wear*, **222**(1), 29–37.
- (35) Guo, F., Wong, P. L., Fu, Z., and Ma, C. (2010), "Interferometry Measurement of Lubricating Films in Slider-On-Disc Contacts," *Tribology Letters*, **39**(1), 71–79.
- (36) Su, B., Huang, L., Huang, W., and Wang, X. (2018), "Observation on the Deformation of Dimpled Surface in Soft-EHL Contacts," *Tribology International*, **119**, 521–530.
- (37) Huang, W., Jiang, L., Zhou, C., and Wang, X. (2012), "The Lubricant Retaining Effect of Micro-Dimples on the Sliding Surface of PDMS," *Tribology International*, **52**, 87–93.
- (38) Chen, L. J., Hsu, C. H., and Yeh, M. C. (2007), "Application of Microcontact Printing to Electroless Plating for the Fabrication of Microscale Silver Patterns on Glass," *Langmuir*, **23**, 12111–12118.
- (39) Olver, A. V., Fowell, M. T., Spikes, H. A., and Pegg, I. G. (2006), "Inlet Suction, a Load Support Mechanism in Non-Convergent, Pocketed, Hydrodynamic Bearings," *Proceedings of the Institution of Mechanical Engineers, Part J: Journal of Engineering Tribology*, **220**(2), 105–108.
- (40) Fowell, M., Olver, A. V., Gosman, A. D., Spikes, H. A., and Pegg, I. (2007), "Entrainment and Inlet Suction: Two Mechanisms of Hydrodynamic Lubrication in Textured Bearings," *Journal of Tribology*, **129**(2), 336.

## Appendix: Derivation of the negative correlation between interference intensity of bright fringes and film thickness

Figure S1 gives the measurement principles of the interferometry in this article. The incident light of wavelength  $\lambda$  is projected perpendicularly onto the lubricated soft contact of film thickness  $h$ . Beams 1 and 2 are those first reflected light from the beam splitter and the slider surface, respectively. The interference intensity  $I$  versus the film thickness  $h$  follows a cosine relationship,

$$I \propto I_1 + I_2 + \sqrt{I_1 I_2} \cos\left(\frac{2\pi}{\lambda} h\right) \quad [\text{S-1}]$$

where  $I_1$  and  $I_2$  are the intensities of beams 1 and 2, respectively.

Bright fringes are obtained when  $h = N \bullet \lambda (N = 0, 1, 2, 3, \dots)$ , so the interference intensity  $I$  for bright fringes can be expressed as follows:

$$I \propto I_1 + I_2 + \sqrt{I_1 I_2} \quad [\text{S-2}]$$

As the reflected beam 2 pass through the film, the intensity  $I_2$  can be formulated as

$$I_2 = I_0 e^{-2h} \quad [\text{S-3}]$$

where  $I_0$  is the intensity of incident light and  $\alpha$  is the light absorption coefficient for lubricant oil.

Thus, the interference intensity  $I$  for bright fringes can be restructured as follows:

$$I \propto I_0 e^{-2h} \quad [\text{S-4}]$$

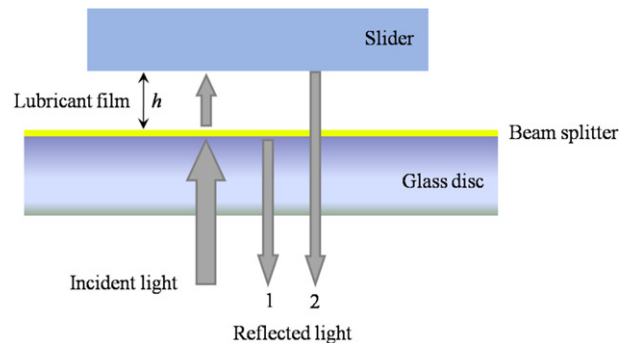


Figure S1. Measurement principles of the interferometry.